Results in Physics 59 (2024) 107549

Contents lists available at ScienceDirect

Results in Physics

journal homepage: www.elsevier.com/locate/rinp

Adjusting the gas detection characteristics of $NiFe_2O_4$ spinel ferrite nanoparticles through the introduction of Zn doping

Eman A. Alghamdi, Refka Sai *

Department of Physics and Astronomy, King Saud University, Riyadh, 11451, Saudi Arabia

ARTICLE INFO

Keywords:
Ni-Zn ferrites
Electron paramagnetic resonance
Mossbauer
Ferromagnetism

ABSTRACT

Nickel ferrite nanoparticles doped with zinc were synthesized at a lower reaction temperature of 180 °C. The research delved into their structural, optical, dielectric, and magnetic properties. These nanoparticles exhibited a distinct cubic spinel structure, with crystallite sizes ranging from 33 to 51 nm. FTIR analysis revealed metal oxide stretching vibrations between 400–600 nm. FESEM and HR-TEM examinations unveiled irregularly shaped nano-particles. XPS analysis disclosed the chemical states of Zn^{2+}, Fe^{3+}, and Ni^{2+} ions. Mossbauer spectra exhibited two sextet patterns related to tetrahedral (A) and octahedral (B) sites, plus a weak doublet pattern. Magnetic tests showed a decrease in saturation magnetization (Ms) but an increase in remanent magnetization (Mr) and coercivity (Hc) values upon doping.

Introduction and preliminaries

In contemporary research, there is a concerted focus on ferrite materials owing to their distinctive physical attributes encompassing optical, electrical, and magnetic characteristics. Ferrites play a crucial role in various applications such as ferrofluids, devices with high and low permeability, microwave devices, high-density storage units, and magnetic drug delivery systems, highlighting their versatility and diverse utility [1–16,16–58]. The significance of ferrites in magnetic materials is underscored by their diverse applications, ranging from ferrofluids, high and low permeability devices and microwave devices to high-density storage units and systems for magnetic drug delivery marks a shift with no commonality in their nature and purpose [1]. However, the current scholarly curiosity about ferrites. is particularly oriented towards investigating their gas sensing capabilities. Ferrites, composite materials composed of iron and metal oxides, exhibit notable properties such as dielectric behavior and high electrical resistivity, coupled with inherent ferrimagnetic traits. Classifiable into four categories—hexagonal, orthoferrite, spinel, and garnets—ferrites present a spectrum of structural variations. Notably, spinel ferrites stand out for their distinctive attributes, including substantial, coercivity (Hc), magnetocrystalline anisotropyelevated, saturation magnetization (Ms), and an elevated Curie temperature [1]. The magnetic and structural attributes of spinel ferrites are intricately influenced by magnetic interactions and the distribution of cations across B and A sites. Within the category of inverse spinel, nickel ferrite exhibits ferromagnetic behavior, characterized by the general formula $[Fe^{3+}]A[Ni^{2+}\ Fe^{3+}]BO_4$. In this formulation, Fe^{3+} is situated at both the B-site and A-site, while Ni^{2+} exclusively takes up the B-site. Notably, nickel ferrite manifests elevated electrical resistivity, coupled with reduced eddy current dissipation [2]. The introduction of Zinc doping into nickel ferrite results in enhanced electrical conductivity, tunable behavior, and broad-ranging applications across diverse fields such as catalysis, biomedicine, and energy storage [3]. The substitution of nickel ferrites with various elements such as Cu, Zn, Co, Ce, among others, imparts remarkable versatility and technological significance to this soft ferrite material. The heightened importance arises from their remarkable ferromagnetic attributes., minimal dissipation due to eddy currents., chemical resistance under electrical conditions, and noteworthy sensor capabilities [4–6]. When Zinc (Zn) is introduced as a dopant into the matrix of $NiFe_2O_4$ at the nickel location. (A site), it has the potential to partially occupy the B site at the nano level. The presence of cations distributed across both A and B sites distinctly impacts the magnetic attributes [10]. Furthermore, during the sintering/calcination process of ferrite materials, zinc ions within the matrix may lose Their placement, leading to the occurrence of unsaturated oxygen ions or cation vacancies. These changes can subsequently impact the overall magnetism of the ferrites [11,12]. Notably, Ni–Zn ferrites are known for their strong magnetic saturation, minimal coercivity, and strong permeability [13], making them particularly suitable for various industrial applications. Several synthesis techniques have been explored for Ni–Zn ferrites, including simultaneous precipitation [14], milling by ball impacts [15], methods involving mechanical action and micro-emulsion pathways [16], solid-state reaction [18], sol–gel [15–61], and techniques employing combustion

* Corresponding author.
E-mail addresses: ialghamidi@ksu.edu.sa (E.A. Alghamdi), refkasai@hotmail.com (R. Sai).

https://doi.org/10.1016/j.rinp.2024.107549
Received 4 February 2024; Received in revised form 2 March 2024; Accepted 5 March 2024
Available online 6 March 2024

in a solution [19]. Among these methods, the solution combustion approach stands out due to its simplicity, ease of processability, and cost-effectiveness in achieving good stoichiometry [19]. In this study, we employed the solution combustion method to fabricate nanoparticles of Ni–Zn ferrite, utilizing as a fuel oxylyl-dehydrazide (ODH). ODH, chosen for its minimal ignition temperature and combustibility attributed to the presence of the N–N bond, undergoes an exothermic decomposition to produce N_2 ($N \equiv N$). This method was deemed suitable for the synthesis of ferrites. The hydrothermal method, characterized by utilizing water at elevated temperatures and pressures to conduct chemical reactions, emerges as a versatile and widely adopted technique. Its advantages include exact management over pressure, temperature, and other parameters, suppression of impurities and by-products leading to a pure final product, reduced energy requirements compared to high-temperature methods, environmental friendliness by minimizing dangerous solvents and the generation of waste, and scalability for industrial production. The hydrothermal method proves invaluable for large-scale synthesis of diverse materials, offering benefits regarding regulation or management, purity, and tailoring material characteristics for particular applications. Thomas Dippong and colleagues found that $Ni_{0.5}Mn_{0.5}Fe_2O_4$ has excellent sonophotocatalytic activity against RhB solution [62]. They discovered that samples with low Ni content have pores of 100 Å, while those with high Ni content have pores of 50 Å. Additionally, they observed that the SiO_2 matrix behaves diamagnetically with a small ferromagnetic fraction, but when $Ni_{0.6}Mn_{0.4}Fe_2O_4$ is embedded in the SiO2 matrix, it exhibits superparamagnetic behavior, contrasting with its high-quality ferromagnetic behavior when unembedded [63]. Recent research has concentrated on electrochemical supercapacitors due to their promising applications in energy storage devices, given their excellent reversibility, high cycling stability, and power density. Transition metal oxides, exhibiting reversible and fast faradaic redox reactions involving chemical processes with electron and ion participation in charge/discharge storage mechanisms, serve as promising electrode materials for supercapacitors. In the realm of gas sensing applications, ferrite-based sensors play a crucial function in both quantitative and qualitative assessment of harmful and scentless gases, with the goal of overseeing acceptable levels in the nearby surroundings and bolstering safety via integrated alarm systems. The limited specificity of unfettered ferrite concerning particular gases can be addressed through the process of choosing appropriate dopants, co-dopants, and formation routes. Diverse spinel ferrites, encompassing a range of types, $NiFe_2O_4$, $ZnFe_2O_4$, $CuFe_2O_4$, and $CdFe_2O_4$, have been extensively investigated for varied applications for detecting gases. Notably, nickel ferrite nanoparticles, while garnering recognition due to their improved magnetic characteristics, have limited information available concerning their aptitude for gas detection, especially in the identification of reducing gases. Reducing gases, such as liquified petroleum gas, have practical implications in various settings, including homes, cars, and storage tanks, necessitating advanced sensors for leak detection. Ferrite materials find utility in remote sensing, magnetic sensing, gas sensors and rotational speed sensors. The global ferrite magnetic material market is poised for substantial growth in the foreseeable future. This growth is primarily propelled by the escalating demand for ferrite magnets across diverse applications including electric motors, magnetic separators, loudspeakers, and computer hard drives. The expansion of the automotive industry, particularly in emerging markets, further augments market demand as ferrite magnetic materials find extensive usage in automotive components like sensors, motors, and power steering systems. Additionally, the surge in renewable energy sources like wind energy drives the need for ferrite magnets in wind turbines. Moreover, the burgeoning electronics sector and the rising adoption of consumer electronics devices contribute to market growth. The market is witnessing a transition towards energy-efficient ferrite magnets, spurred by environmental regulations and the pursuit of sustainable solutions. Manufacturers are investing in research and development endeavors to enhance ferrite magnetic materials' performance characteristics while simultaneously reducing their weight and size. Furthermore, there is a notable uptick in the adoption of soft ferrite materials, offering superior magnetic properties and enhanced frequency performance compared to traditional hard ferrite materials. This trend is propelled by the escalating demand for high-frequency applications in various sectors including telecommunications, consumer electronics, and medical devices. Overall, driven by global imperatives such as sustainability, energy efficiency, and technological advancements, the ferrite magnetic material market is poised to sustain robust growth. Market projections suggest a compounded annual growth rate (CAGR) of The innovation in this research involves creating nanoparticles of Zinc-substituted $NiFe_2O_4$ through a straightforward hydrothermal method at a reduced reaction temperature and a brief duration. The size and form of the particles are regulated by various operational factors such as temperature, level of dopant, and pH. This investigation seeks to enhance the chemical makeup of Zinc-replaced nickel ferrite nanoparticles with specific structural, microstructural, and physicochemical attributes suited for use in supercapacitors and gas sensors. The particles produced are examined using X-ray Diffraction (XRD), Fourier Transform Infrared Spectroscopy (FTIR), Raman spectroscopy, X-ray Photoelectron Spectroscopy (XPS), Field Emission Scanning Electron Microscopy (FE-SEM), High-Resolution Transmission Electron Microscopy (HR-TEM), in addition to evaluations of their optical, magnetic, and dielectric characteristics.

Table 1
The number of moles of all reagents used in the synthesis.

Sample	x	$Zn(NO_3)_2 6H_2O$	$Ni(NO_3)_2 6H_2O$	$Fe(NO_3)_2 9H_2O$
$NiFe_2O_4$	0	0.005	0.995	1
$Zn_{0.11}Ni_{0.89}Fe_2O_4$	0.11	0.112	0.888	1
$Zn_{0.33}Ni_{0.67}Fe_2O_4$	0.33	0.331	0.669	1
$Zn_{0.52}Ni_{0.48}Fe_2O_4$	0.52	0.520	0.480	1

Empirical investigation

Experimental details

The precursor compounds, namely Iron nitrate nonahydrate (99% pure), nickel nitrate hexahydrate (99% pure), and zinc nitrate hexahydrate (99% pure) were utilized, were procured from Sigma Aldrich (India) with a certified purity of 99.9%. The acquired chemicals were employ acquired ed without undergoing supplementary purification processes.

Nanoparticle synthesis protocol for $Zn_xNi_{1-x}Fe_2O_4$

The synthesis of Zinc-substituted $NiFe_2O_4$($Zn_xNi_{1-x}Fe_2O_4$) nanoparticles with varying concentrations of x was conducted through a hydrothermal route. The precursors, Iron nitrate nonahydrate, nickel nitrate hexahydrate, were separately dissolved in distinct beakers and stirred thoroughly for a duration of 30 min. Following the stirring process, the liquid mixtures were combined in a single beaker, and sodium hydroxide (NaOH, 1.1 M) was gradually added slowly in drops. The resultant mixture underwent stirring for approximately 35 min before being exposed to a heat of 180 °C for a duration of 7 h within a hot air oven. Subsequently, the brown-colored purified sediment was subjected to drying at 85 °C for approximately 4 h. The synthesis of Zinc-doped $NiFe_2O_4$ nanoparticles are listed in Table 1.

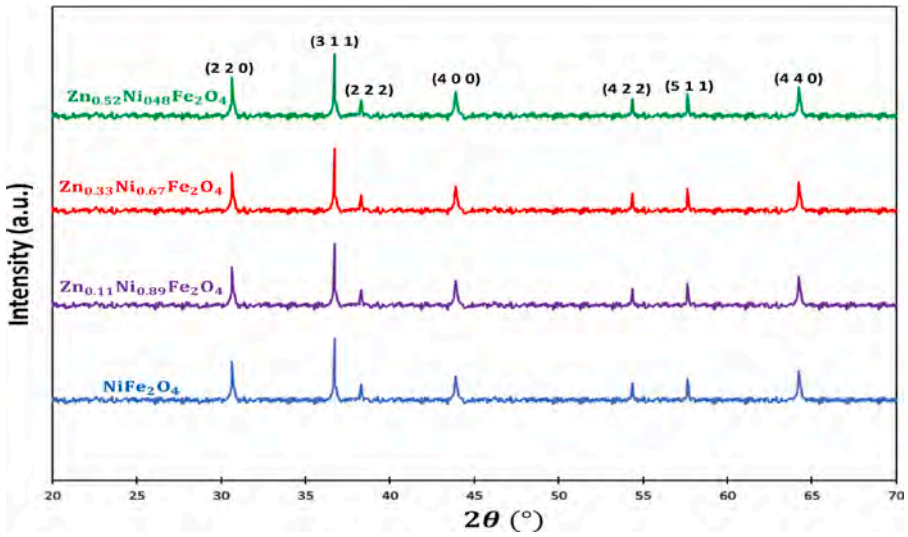

Fig. 1. XRD diagram of $Zn_xNi_{1-x}Fe_2O_4$ nanoparticles for different x ($x = 0.0$, 0.11, 0.33 and 0.52).

Analytical methods for characterization

The evaluation of Zinc-substituted $NiFe_2O_4$ nanoparticles encompassed a comprehensive analysis of their crystal structure, phase purity, and degree of crystallinity through X-ray Diffraction (XRD), utilizing CuKα radiation with a wavelength of 1.5414 Å(XPertProPW3050/60). The identification of operative groups was studied using Fourier Transform Infrared (FTIR) spectroscopy on a Thermo Nicolet iS5 instrument. Raman spectroscopy, performed on a WiTech alpha 300 within the range of 100–800 cm^{-1}, was employed to investigate Raman-active modes. The particle surface morphology and size were examined utilizing Field Emission Scanning Electron Microscopy (FESEM) with a Zeiss SUPRASS-SEM instrument and High-Resolution Transmission Electron Microscopy (HR-TEM) with a FEI-TECNAI G2Twin instrument, respectively. Optical characteristics were acquired utilizing a SHIMADZU 2600 instrument. The X-ray Photoelectron Spectroscopy (XPS) measurements were executed utilizing an electron spectrometer (PHI5000). Dielectric characteristics were explored at typical ambient temperature utilizing the Hio-Ki-Im356 model. isomer shift (IS), magnetic hyperfine fields (Hin), and quadrupole shifting (QS) were determined via 57Fe Mössbauer spectroscopy, employing the AVFTB which named Advanced Variable Field Translation Balance instrument. Magnetic behavior was ascertained using the AVFTB instrument.

Finding and discussion

Analysis of structure and functional groups

The X-ray Diffraction (XRD) spectra of Zinc-doped $NiFe_2O_4$ nanoparticles, as illustrated in Fig. 1, reveal distinct peaks at 2θ values of 30.68°, 36.63°, 37.65°, 43.89°,54.39°, 57.69° and 64.15°, corresponding to the plan(220), plan (311),plan (222), plan (400), plan (422), plan (511), and plan(440), respectively. These peaks are indicative of a characteristic structure of cubic spinel. The observed diffraction peaks align consistently utilizing the identification number from the Joint Committee on Powder Diffraction Standards (JCPDS) card (85–4929), affirming the symmetry group Fd3m (No. 225). The increase in Zinc content is accompanied by a corresponding augmentation in the intensity of the significant peaks, signifying the inclusion of Zinc with the $NiFe_2O_4$ change lattice. This augmentation is attributed to the higher atomic number of Zinc (30) in comparison to nickel (28). The distinct diffraction peaks observed for $NiFe_2O_4$ $Zn_xNi_{1-x}Fe_2O_4$ nanoparticles are indicative of good crystallinity particles [24]. Additionally, the lack of any supplementary peaks attests to the purity of the obtained nanoparticles. The A subtle alteration in the location of peaks is discernible with an increase in zinc content, as depicted in the inset of Fig. 1. This shift is attributed to the modest variance in ionic radii in the middle the replacing constituent Zn^{2+} and the host element Ni^{2+}, amounting to 4.36%. The most prominent observation among the reflections is the dominance of the (311) reflection, serving as confirmation of the formation of the spinel phase during combustion. Additionally, a notable trend emerges as the concentration of Zn increases: the peak corresponding to (311) exhibits a discernible shift towards lower diffraction angles (2θ). The application of Scherrer's formula allows for determining the size of the crystal particles, following the expression [7]:

$$D = \frac{0.891\lambda}{\beta \cos\theta} \tag{1}$$

In the aforementioned expressions, $\varepsilon\lambda\varepsilon$ represents the wavelength, $\varepsilon\beta\varepsilon$ denotes the FWHM (full width at half maximum), "D" signifies the size of crystallite size, and $\varepsilon\theta\varepsilon$ corresponds to Bragg's angle. It is noteworthy that the escalation in zinc content contributes to a diminution in grain growth, primarily attributed to the segregation of grain boundaries, which in turn impedes the mobility of grains [23]. The lattice parameter was established through the application of the following equation[4]:

$$a = \sqrt{h^2} + \sqrt{k^2} + \sqrt{l^2} \tag{2}$$

In the aforementioned equation, "a" represents the lattice constant, "d" signifies the interplanar spacing, and "hkl" presents the Miller indices. The lattice constant undergoes a marginal large from 8.3692 to 8.4957 Å, as evidenced by the experimental data. As per the findings reported by Mahalakshmi et al. the observed augmentation in lattice constant is primarily associated with the comparatively increased ionic radius of Zn^{2+} (0.76 Å) in contrast to Ni^{2+} (0.68 Å) [25]. The substitution of Ni^{2+} with Zn^{2+} induces an escalation in regional structural irregularity, consequently resulting in a decrease in crystal size. The parameters of dislocation density δ, microstrain, and ϵ X-ray density ρ are ascertained through the following relations [16]:

$$\delta = \frac{1}{D^2} \tag{3}$$

$$\rho = \frac{8M}{N \times a^3} \tag{4}$$

$$\epsilon = \frac{\beta \cos\theta}{4} \tag{5}$$

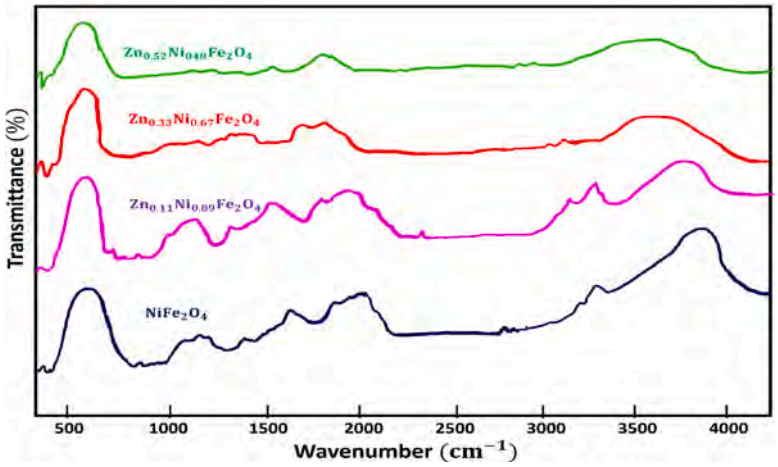

Fig. 2. FTIR spectrum of $Zn_xNi_{1-x}Fe_2O_4$.

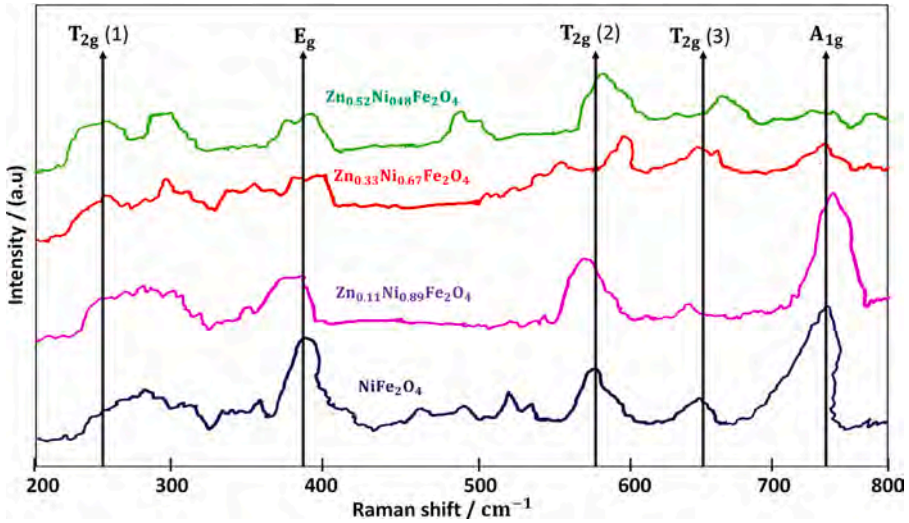

Fig. 3. Raman spectra for $Zn_xNi_{1-x}Fe_2O_4$ nanoparticles for different x ($x = 0.0$, 0.11, 0.33 and 0.52).

Table 2
The parameters of structural, encompassing lattice constant, dislocation density, crystallite size, and strain, are characterized by their respective values. These values are contingent upon the doping content of the samples.

Doping concentration	0.00	0.11	0.33	0.52
Samples	$NiFe_2O_4$	$Zn_{0.11}Ni_{0.89}Fe_2O_4$	$Zn_{0.33}Ni_{0.67}Fe_2O_4$	$Zn_{0.52}Ni_{0.48}Fe_2O_4$
Lattice a (∀) In literature [64]	8.34562	8.37106	8.38466	8.40019
Obtained Lattice a Å	8.3692	8.3927	8.4136	8.4957
D±1 nm	43	39	35	31
$\delta \times 10^{15}(lines/m^2)$	5.6726	6.2657	6.5640	6.8345
$\rho(gm/cm^3)$	5.33	5.31	5.29	5.27
$\epsilon \times 10^{-3}$	0.58	0.74	0.85	1.04

In accordance with Table 2, the weight of the molecular sample denoted as "M" and the Avogadro number represented by "N" are significant parameters. Upon the introduction of Zinc (Zn) as a substitute, the density of $NiFe_2O_4$ exhibits a decline attributable to the larger ionic radii [7]. Concurrently, the dislocation microstrain and density experience an escalation concomitant with the reduction in crystallite size. The determined lattice constants for the various samples exceed those reported by Anupama MK et al. [64], thus affirming the successful incorporation of Zn into Ni and the attainment of a well-defined crystalline structure.

Wherein r_1 and r_2 denote the radii of sites, d_T and d_0 represent the bond lengths of the B-site and A-site, respectively, H_2 and H_1 signify the hopping lengths, d_1 indicates the common border in the A-site, and d_2 and d_{12} denote the common and exclusive edges in the B-site. The negative ion parameter is established at 0.383 Å, while r_0 signifies the ion radius of oxygen at 1.31 Å. The computed values for Zn-substituted $NiFe_2O_4$ are tabulated in Table 3. The observed augmentation in lattice values with an escalating zinc percentage primarily arises from the disparity in ionic radii in the middle of Ni^{2+} and Zn^{2+} ions, along

Table 3
Progression of Structural Parameters for $Zn_xNi_{1-x}Fe_2O_4$ in Relation to the Variation in Zinc Content.

Dopant percentage	0.00	0.11	0.33	0.52
Sites radii (∀) $r_1 = a\sqrt{3}(U-0.25) - r_0$	0.253	0.267	0.276	0.296
Sites radii (∀) $r_1 = a(0.625-U) - r_0$	0.567	0.579	0.587	0.623
Bond length (∀) $d_T = a\sqrt{3}(U-0.25)$	1.481	1.491	1.497	1.508
Bond length (∀) $d_0 = a\sqrt{3U^2 - \frac{11}{4} + \frac{43}{64}}$	3.234	3.237	3.311	3.335
Hoping length (∀) $H_1 = a\sqrt{3}\times 0.25$	2,627	2.681	2.695	2.710
Hoping length (∀) $H_2 = a\sqrt{2}\times 0.25$	2.144	2.153	2.178	2.187
Sites edges (∀) $d_1 = a\times 1.414(2U-0.5)$	2.421	2.427	2.435	2.451
Sites edges (∀) $d_2 = a\times 1.414(1-2U)$	1.731	1.841	1.854	1.871
Sites edges (∀) $d_{12} = a\sqrt{4U^2 - 3U + \frac{11}{16}}$	2.090	2.141	2.153	2.174

with the ensuing cation redistribution [26]. Notably, the radii of site (r_1 and r_2) and hopping lengths (H_1 and H_2) exhibit an increase upon zinc substitution due to the redistribution of cations characterized by distinct ionic radii [8]. The FTIR (Fourier-transform infrared spectroscopy) analysis, depicted in Fig. 2, delineates the vibrational characteristics of Zn-substituted $NiFe_2O_4$ nanoparticles under normal room conditions within the spectral from 4000 to 450 cm^{-1}. The discerned broad and attenuated bands at approximately 3439 cm^{-1} and 1645 cm^{-1} correspond to bending vibrations and the elongation of H–O–H, signifying the presence of water absorbed from the ambient atmosphere. At 2925–2937 cm^{-1}, the band observed is attributed to Zn–H vibration, while the range of 1370–1410 cm^{-1} is associated with Zn–O elongation vibration. The FTIR analysis validates the preferential stabilization of Ni^{2+} ions within octahedral crystal fields, while Zn^{2+} ions tend to occupy tetrahedral sites due to their inclination towards forming covalent bonds. The spectra exhibit distinctive absorption bands characteristic of spinels, with bands attributed to tetrahedral and octahedral metal stretching observed around 650–570 cm^{-1} for Zn^{2+} and Ni^{2+} ions, respectively, while the remaining positions are filled by 16 Fe^{3+} ions.

The bands of metal oxide originating from the B and A sites of pristine $NiFe_2O_4$ nanoparticles are represented by peaks at 589 and 422 cm^{-1}, respectively. Upon substituting Zn^{2+} for the host Ni^{2+}, the inherent elongation vibrations of the oxide-metal in the B-site and A-site undergo upward shifts to greater wavenumbers, specifically within the ranges of 594–605 and 426–431 cm^{-1}, respectively. This phenomenon is ascribed to the greater mass atomic of Zinc ions compared to Ni^{2+} ions [27]. Bid et al. posited that alterations in peak positions and relative intensities are attributable to variations in lattice values and the crystalline effect resulting from the substitution of primary constituents with foreign elements possessing disparate ionic radii and atomic numbers [30]. The heightened intensity of peaks with augmenting Zn percentage is attributed to alterations in the Fe–O band upon the addition of Ni by Zn [28]. Within the 39 vibrational forms of Raman for the structure of mono-phase spinel, particularly 3 T_{2g}, A_{1g}, and E_g, aligned with the space group (Fd-3 m), five are discerned as active. In the inverse spinel structure, A-sites (tetrahedral) are partially occupied by Fe^{3+} and Zn^{2+}, while B-sites are filled with Fe^{3+}, Zn^{2+} and Ni^{2+}. Fig. 3(a-d) illustrates the obtained Raman spectrum for both pure and zinc-doped $NiFe_2O_4$ nanoparticles, with corresponding calculated parameters detailed in Table 3. The topmost band of frequency band, A_{1g} modes, is credited to the elongation motion of ions of oxygen with Fe–O bonds in the A-site. The symmetrical flexing of M ions alongside oxygen atoms is associated with E_g forms. T_{2g} (1) forms arise from the movement in translation of four oxygen atoms connected to metal ions in the tetrahedral site. T_{2g} (3) and T_{2g} (2) are ascribed to bending vibrations and asymmetric elongation of metal ions and oxygen atoms in the octahedral site. The obtained peak shifts towards greater wave numbers are attributed for the rearrangement of cations within octahedral and tetrahedral sites [1]. The shifts in peaks, coupled with increases in intensity and width, as outlined in Table 3, are primarily ascribed for the rearrangement of cations and the influence of particle dimension (size).

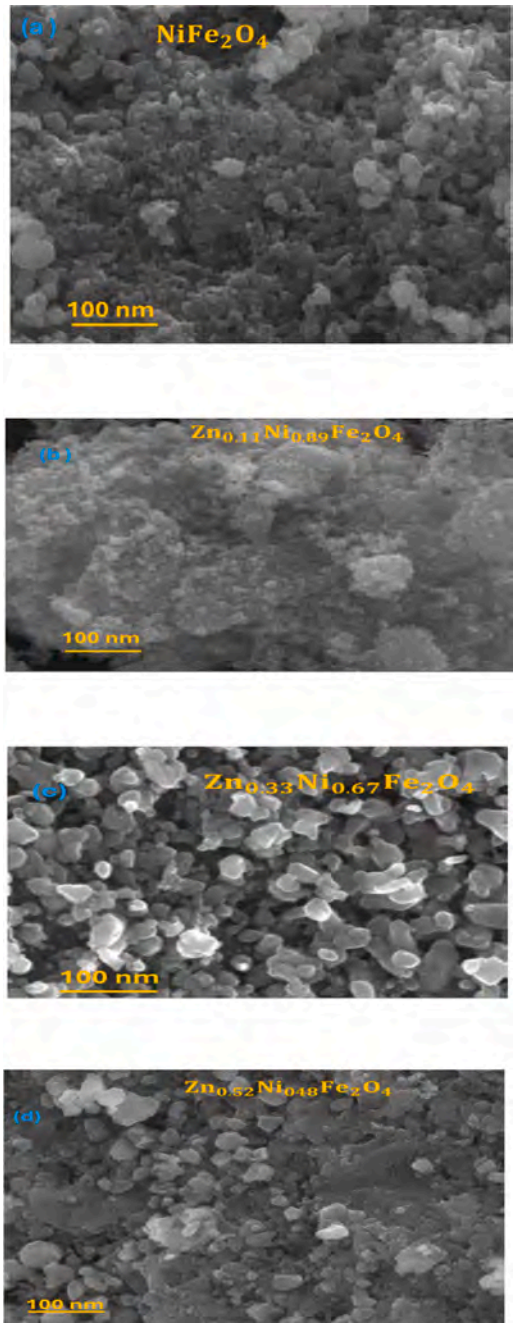

Fig. 4. FESEM images of $Zn_xNi_{1-x}Fe_2O_4$.

Analyses on morphology

Fig. 4 presents the characterization of particle morphology and size within the $Zn_xNi_{1-x}Fe_2O_4$ system as a function of zinc content. The field-emission scanning electron microscopy (FESEM) graphs in Fig. 4 (a–d) depict irregularly shaped particles exhibiting an uneven size distribution and a propensity for clustering [28]. The observed agglomeration can be attributed to higher surface energy and the influence of the dehydration process during nanoparticle fabrication, as elucidated in literature [29]. The distribution of particle sizes,as depicted in Fig. 4(e–h), showcases a relatively tight average size ranging from 37 to 51 nm. Notably, the particle size and morphology distribution remain largely unaffected by zinc doping and its content. Fig. 5 provides high-resolution transmission electron microscopy (HR-TEM) graphs of representative $Zn_{0.52}Ni_{0.48}Fe_2O_4$ nanoparticles, along

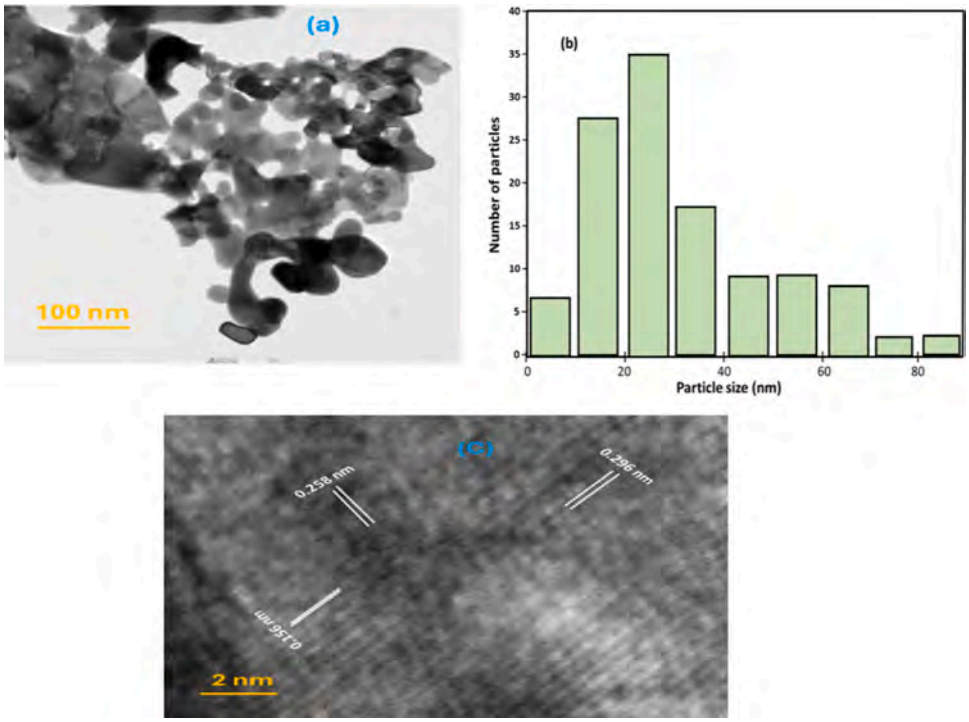

Fig. 5. (a) HR-TEM images of representative $Zn_{0.52}Ni_{0.48}Fe_2O_4$ nanoparticles for $x = 0.5$, (b) particle size distribution and (c) Fringe pattern.

with the corresponding the distribution of particle size, selected are of electron diffraction (SAED) diagram, and fringe diagram. Within the confines of Fig. 5(a), a lone nanoparticle is displayed. Upon closer examination of Fig. 5(a), a notable pattern emerges: the nanoparticles exhibit a uniform dispersion within the nano-scale spectrum, ranging from 30 to 165 nanometers, with an average particle dimension of 51 nanometers, as depicted in Fig. 5(b). This observation underscores the consistent distribution of particles across the nano-scale spectrum. In Fig. 5a, nanosized cubic-shaped particles are discerned, with evidence of agglomeration where smaller particles adhere to larger ones. This agglomeration phenomenon is attributed to weak Vander Waals forces and magnetic interactions between particles, where each nanoparticle acts as a magnet, leading to mutual attraction [28]. The average size of grain for the Zn-NF3 sample is determined to be approximately 38 nm, as inferred from the histogram in Fig. 5b. This grain size measurement from HR-TEM aligns within the particle size values Found from FESEM and the crystal size determined by XRD studies [28].

The SAED diagram (Fig. 5c) exhibits diffraction circles associated with various planes, affirming the polycrystalline characteristics of the examined powder, a finding consistent with the XRD diagram. The patterns of fringes, with distinct d-spacing values of 0.298, 0.251, and 0.146 nm (Fig. 5d), align with the plane (220), plane (311), and plane (440) for structure cubic, further confirming the crystalline nature as corroborated by XRD studies. The TEM image elucidates the high-quality crystalline structure of Zn-doped ferrite, particularly in the case of $Zn_{0.52}$ $Ni_{0.48}$ Fe_2 O_4. This underscores the favorable characteristics of Zn-doped ferrite, rendering it a promising candidate for various applications.

Optic properties

The optic characteristics of the obtained Zn-substituted $NiFe_2O_4$ nanoparticles are scrutinized through UV-DRS, as depicted in Fig. 6a. Examination of the absorption spectra reveals a discernible move toward shorter wavelengths, indicative of an augmentation in the value of band gap [15]. We have Tauc's equation, expressed in [31] as

$$(\alpha h\nu)^2 = A(h\nu - E_g),$$

where A is the factor of proportionality (constant), $h\nu$ denotes the energy of the photon, α represents the coefficient of absorption, and E_g signifies the energy of band-gap, is employed to calculate the band-gap energy. Extending the curve graphed between $(\alpha h\nu)^2$ and $(h\nu)$ yields the band-gap values, as illustrated in Fig. 6(b–e). The computed optical band-gap obtained for $NiFe_2$ O_4, $Zn_{0.11}$ $Ni_{0.89}Fe_2$ O_4, $Zn_{0.33}$ $Ni_{0.67}Fe_2$ O_4, $Zn_{0.52}$ $Ni_{0.48}Fe_2$ O_4 are 1.57, 1.65, 1.73, and 1.96 eV. Notably, a conspicuous escalation in energy band gap is observed with an increase in Zn content. The widening of the bandgap is attributed to the reduction in crystallite size and the consequential quantum confinement effect [32]. The bandgap values derived from Fig. 6(b–e) are consistent with obtained measurement explained in the literature [23]. The discerned small band-gap values underscore the suitability of the investigated $Zn_xNi_{1-x}Fe_2$ O_4 sequence of compounds for applications in opto-electronic devices.

X-ray photoelectron spectroscopy (XPS) finding

To validate the elemental makeup and ascertain the oxidation conditions of the constituent elements, X-ray photoelectron spectroscopy (XPS) analysis was conducted on the specified composition $Zn_{0.52}Ni_{0.48}$ Fe_2 O_4, as illustrated in Fig. 7. Notable signals with binding energies at 285.6, 531.5, 713.8, 723, 858, 877.5, 899.5, and 905 eV were noticed and recognized as O1s,Zn1s,$Fe2p_{3/2}$, $Fe2p_{1/2}$, $Ni2p_{3/2}$, $Ni2p_{1/2}$, $Zn2p_{3/2}$, and $Zn2p_{1/2}$ emissions. Peaks corresponding to $Fe2p_{3/2}$ at 711.58 and 713.70 eV suggested the existence of Fe^{3+} in B and A sites, with the additional peak at 723.88 eV ascribed to $Fe2p_{1/2}$. The existence of the peak of satellite between $Fe2p_{3/2}$ and $Fe2p_{1/2}$ exclusively pertained to Fe^{3+} ions [16]. The Ni 2p signal exhibited deconvolution with several peaks at 854.8, 857.7, 858.6, 874.5, and 875.6 eV. Satellite peaks noticed at 862.3, 878.5, and 881.9 eV were indicative of Ni^{2+} [32]. Peaks noticed at 931.3, 933.1, and 934.6 eV, together with peaks of satellite at 941.6 and 942.5 eV, were attributed to $Zn2p_{3/2}$. Peaks noticed at 953.7 and 955.3 eV, together with a peak of satellite at 961.7 eV, associated to $Zn2p_{1/2}$, confirming the presence of Zn^{2+}, in alignment with previous in written works [32]. The peak of Zn1s at

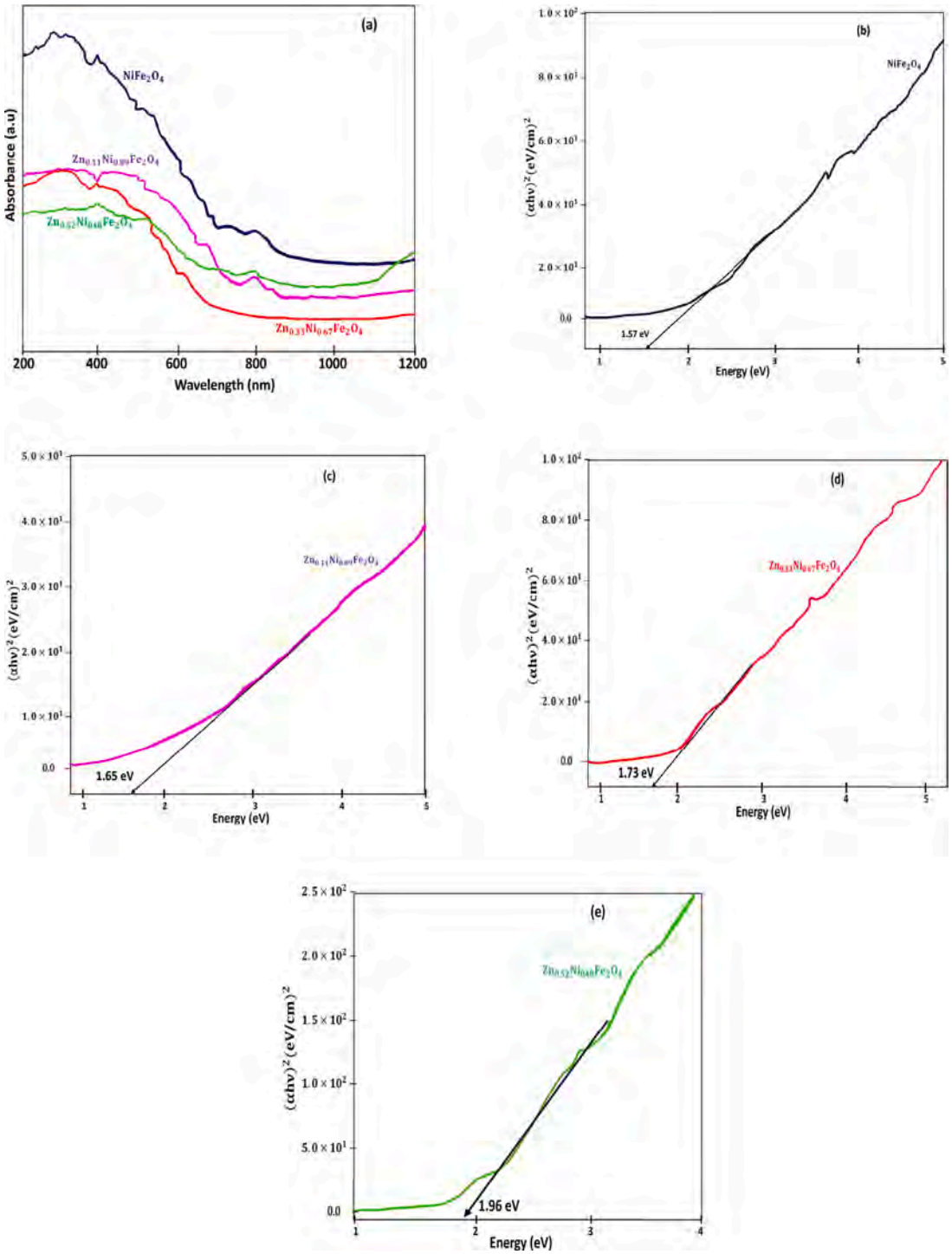

Fig. 6. (a)absorption spectra of $Zn_xNi_{1-x}Fe_2O_4$ nanoparticles and their graph of band gap (b–e).

285.6 eV served as a benchmark for the ongoing XPS assessment [33]. In a manner completely dissimilar, the significant peak at 528.95 eV is ascribed to the presence of atoms of oxygen, while the peak of O3 at 530.37 eV corresponds to the oxygen containing a hydroxyl group vacancy on the nanoparticle surface. The peak denoted as O3 indicates oxygen that has been absorbed, featuring an energy values about of 532.12 eV [16,34]. The wide peak at 975 eV is typically assigned to O Auger, OKLL. No other significant peaks are detected in the XPS spectrum, suggesting the absence of additional elemental compositions and thus confirming the purity of the $Zn_xNi_{1-x}Fe_2O_4$ system.

Dielectric analysis

The dielectric constant of the synthesized nanoparticles is assessed in terms of frequency under normal room conditions, as illustrated in Fig. 8a. The calculation of ϵ' is conducted utilizing the equation

$$\epsilon' = Cd\epsilon^0 A,$$

where "C" represents the pellet capacitance, "d" denotes thickness, "ϵ^0" signifies the dielectric constant of free space, and "A" signifies the area of cross-section [7]. The dielectric constant exhibits a notable increase at low frequency and subsequently decreases with an elevation

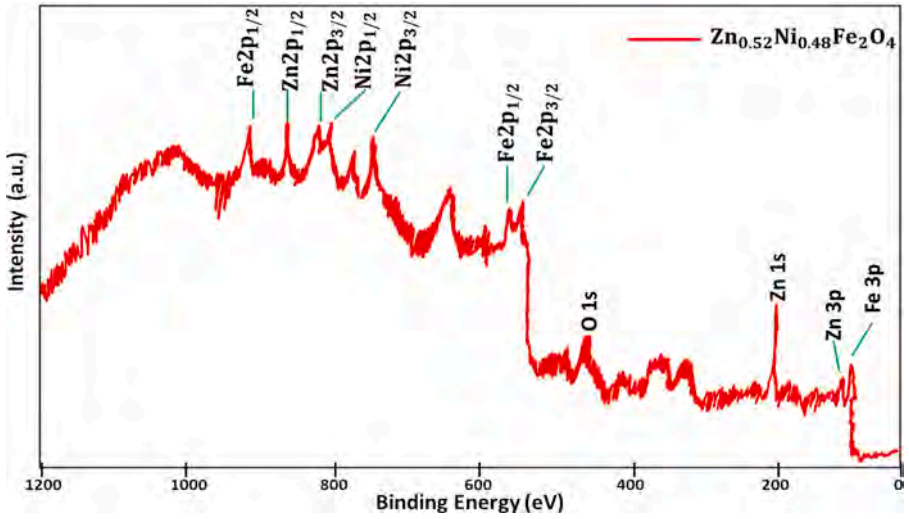

Fig. 7. XPS spectrum of $Zn_xNi_{1-x}Fe_2O_4$.

in frequency (Fig. 8a). At higher frequencies, the dielectric constant reaches a constant value. This frequency-dependent behavior can be elucidated by the polarization due to space charge arising from the inhomogeneous dielectric character of the material. It stems from the existence of well-conducting grains isolated by inadequately conductive inter-grain boundaries. As the frequency of the imposed field increases, the exchange of electrons in the middle of Fe ions may lag behind the applied alternating field, resulting in a decrease in the ϵ' value. The elevated ϵ' value at small frequency is attributed to the existence of microstructural defects and other structure and dislocations [36]. The damping coefficient, arising from the lag in polarization relative to the applied alternating field, is examined in Fig. 8b. The variation of $\tan\delta$ as function of frequency is expressed as

$$\tan\delta = \frac{1}{2\pi f C_p R_p},$$

where "C_p" denotes the capacitor with parallel plates and "R_p" signifies the resistance of parallel plates [7]. The obtained values for the loss factor are 21.43 for $NiFe_2O_4$, 16.05 for $Zn_{0.11}Ni_{0.89}Fe_2O_4$, 5.86 for $Zn_{0.33}Ni_{0.67}Fe_2O_4$, and 3.83 for $Zn_{0.52}Ni_{0.48}Fe_2O_4$. Fig. 8b displays for all samples the emergence of a peak in the frequency area of 5–7 MHz. This peak occurs when the frequency of a condition coincides with the oscillating electric field and the inherent electric charges. The observed peak change towards diminish frequency, coupled with diminish dielectric loss for the $Zn_{0.52}Ni_{0.48}Fe_2O_4$ sample, suggests favorable characteristics for potential applications in antennas and waveguides [37]. The elevated dielectric reduces the maximum number of electrons of pure $NiFe_2O_4$, which is attributed to electrons exchanged in middle of Ni^{2+} and Fe^{3+} ions at the B-site [38]. The observed discrepancies in the reduced element may be attributed to the increase resistive nature of grain boundaries, that has a role a pivotal role in the minimal frequency area. In this area, a certain higher level of energy is needed for electron exchange. between Fe ions, resulting in a higher loss factor. Conversely, at higher frequencies, low-resistance grains play a more significant role in the conduction process, leading to a minimal loss [38]. The connection or association between frequency and AC conductivity is depicted in Fig. 8c. In materials ferrite, the conduction process is driven by the exchange of electrons between Fe^{2+} and Fe^{3+} ion Rotational rate s. The AC conductivity is determined using the relation

$$\sigma_{ac} = \omega\epsilon^0\epsilon'\tan\delta,$$

where "ω" represents angular frequency and "ϵ^0" signifies the electrical permittivity within a vacuum or free space [39]. In the low-frequency region, grain boundaries exhibit increased activity, resulting in a lower exchange of electrons between Fe^{2+} and Fe^{3+}, and consequently, smaller conductivity is observed. When the frequency increases, the rate of transition or movement between charge carriers also rises, leading to an increase in conductivity. Fig. 8: Dielectric properties of $Zn_xNi_{1-x}Fe_2O_4$ nanoparticles with respect to frequency for different concentration x = 0.0, 0.11, 0.33 and 0.52 (a) Dielectric constant, (b) Tangent loss, and (c) AC conductivity

Magnetic analysis

Fig. 9 illustrates the Mössbauer spectra of $Zn_{0.52}Ni_{0.48}Fe_2O_4$ nanoparticles captured under ambient temperature conditions. Mössbauer spectra provides crucial data regarding the occupancy and valency of iron among B and A sites. The figure shows two sextet patterns which relate to one only weak doublet diagram. The distinct appearance of a robust sextet configuration indicates the structured and balanced ferrimagnetic condition of the produced nanoparticles [40]. Additionally, the detection of a subtle pair pattern suggests that the timeframe for the magnetic orientation change within the created nanoparticles is under 12 ns. [40]. The doublet, with an isomer shift (IS) value of 0.22 mm/s and a quadrupole splitting (QS) value of 0.42 mm/s, is attributed to Fe^{3+}. The two distinctive sets of six-fold configurations discovered in this investigation, characterized by IS values of 0.29 and 0.36 mm/s, and Hin values of 46.7 and 49.8 T, are attributed to the presence of Fe^{3+} ions occupying A and B sites correspondingly. The existence of Fe^{3+} in both B and A sites confirms the inverse spinel ferrite structure. The discrepancy in IS values, with the octahedral site registering at 0.38 mm/s and the tetrahedral site at 0.28 mm/s, results from the wider band gap between Fe^{3+}–$O2^-$ bonds situated at the B site compared to those at the A site. Consequently, the decrease in co-valency impact results in an increase in the isomer change value observed at the B-site [41–48]. The lack of a dual pattern associated with ferrous Fe^{2+} ions signal the singular existence of Fe^{3+} ions, confirming the unadulterated nature of the synthesized nanoparticles. Notably, the minute proportion of approximately 1.72% Fe^{2+} identified through XPS analysis does not correlate with the findings obtained from the Mössbauer. In the realm of Ni–Zn ferrite, the minimal isomer shift value indicates a reduced of significant charge impact from s electrons on the tetrahedral Fe^{3+} atom. The assessed isomer shift and quadrupole splittings affirm the trivalent state of Fe in both octahedral and tetrahedral sites, alongside its predominantly high-spin nature. The magnetic characteristics of Zn-substituted $NiFe_2O_4$ nanoparticles are additional explored utilizing alternating field vibrating sample magnetometry (AVFTB) measurements. The hysteresis loops of $Zn_xNi_{1-x}Fe_2O_4$, depicted in Fig. 10a,

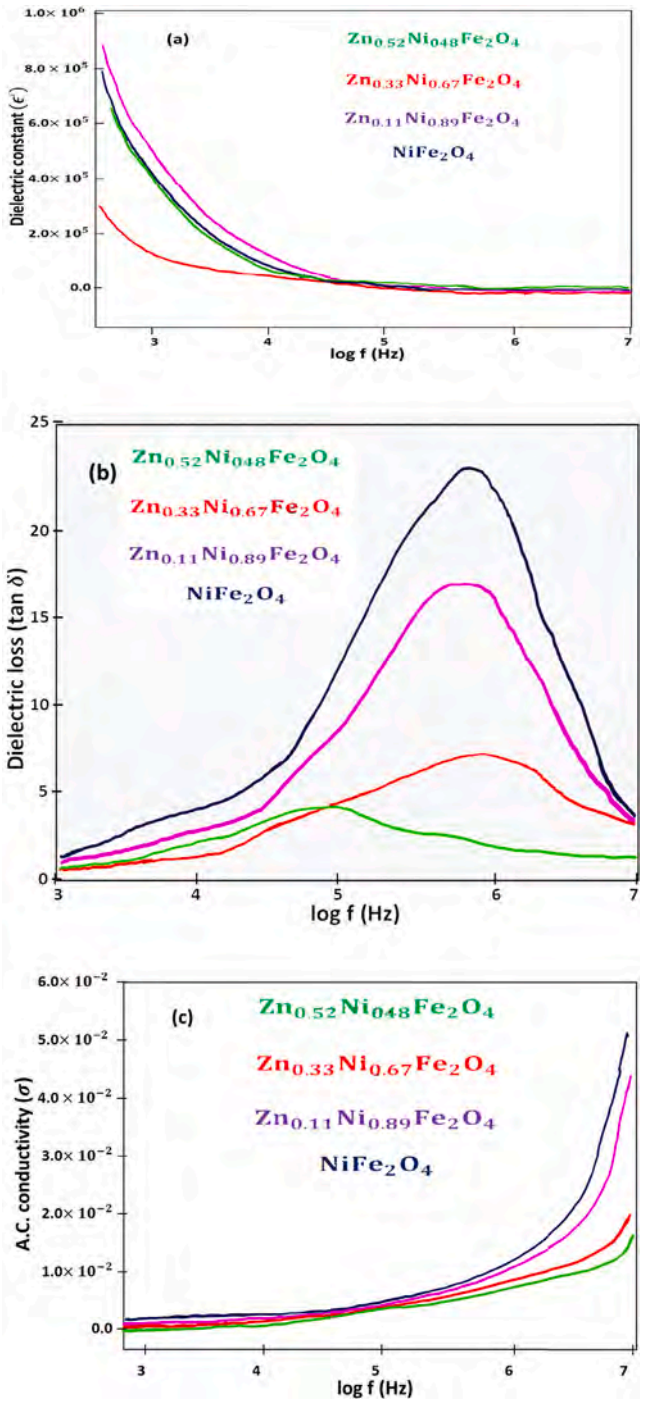

Fig. 8. Dielectric properties of $Zn_xNi_{1-x}Fe_2O_4$ nanoparticles with respect to frequency for different concentration x = 0.0, 0.11, 0.33 and 0.52 (a) Dielectric constant, (b) Tangent loss, and (c) AC conductivity.

indicate a gentle ferromagnetic property. The parameters, including saturation magnetization (M_s), remanent loop squareness (M_r/M_s), magnetization (M_r), coercivity (H_c), Bohr magneton (μB), remanence coercivity (H_{cr}), and the calculated constant of anisotropy (K) from the hysteresis curves. It has been noted that the saturation of magnetization (Ms) diminishes with the rise in zinc content. This decline is due to the fact that the magnetic moment of zinc (2 μB) is smaller compared to that of nickel (3 μB). prevalence of zinc ions mainly resides in the B-sites, although some may also be found in the A-sites. This scenario leads to the migration of Fe^{3+} ions to the octahedral B-sites, ensuring charge equilibrium and maintaining the stoichiometry of the chemical composition. Consequently, a decline in the superexchange interaction between the A and B sites results in a reduction in the magnetization of the B-site sublattice as the zinc content increases [49,50]. As the grain size decreases, the rise in domain walls impedes the material's demagnetization, consequently leading to an escalation in coercivity [51,52]. The developed nanoparticles of magnetic ternary/quaternary oxides are considered appropriate for utilization in various fields, such as microwave technologies, transformer systems, and applications requiring magnetic shielding [42,43]. Backfield assessments were utilized to establish the H_{cr} values. Subsequently, the ratios of M_r/M_s and H_{cr}/H_c were graphically represented in a Day plot diagram [53] to analyze the characteristics of domains within the nanoparticles (Fig. 10b). The findings reveal that all specimens fall within the pseudo-single domain category. The M_r/M_s ratio, termed as loop squareness, fluctuates based on the zinc content. This variation can be linked to magnetic field attributes, imperfections, and anisotropy in the crystal structure [54]. The magnetic momentum and anisotropy constant are derived through the equations $\mu B = M \times M_s/5586$ and $K = H_c \times M_s/0.97$, wherein "M" denotes the molecular weight of nanoparticles composed of zinc-substituted nickel ferrite. All magnetic properties are listed in Table 4. The escalation in values of anisotropy constant correlates with the rise in coercivity, a change primarily linked to phase development and the enlargement of grain structures [55]. As the coercivity value increased, so did the anisotropy constant values, a phenomenon attributed to the evolution of phases and the growth of grains. Specifically, saturation magnetization initially rises with Zn concentration until $x = 0.52$. At $x = 0.52$, the maximum saturation is observed, indicating a limit to the presence of impurities detectable via XRD. Additionally, paramagnetic contributions are noted alongside ferromagnetic properties in Zn-doped Ni ferrite samples, with net magnetization decreasing beyond $x = 0.52$ Zn substitution. The anisotropic constant (K) increases with increasing Zn concentration, suggesting suppression of ferromagnetic nature by paramagnetic influence. The observed ferromagnetism in NiFe2O4 samples may stem from cation distribution and superexchange interactions between Ni and Fe at tetrahedral A and octahedral B sites. Substitution of non-magnetic ions like Zn alters exchange interactions, influencing spin arrangements and magnetic properties. In our study, we observed an increase in the anisotropy constant K with rising Zn content, contrary to the findings of Anupama MK et al. [64], who reported a decrease in this constant with increasing Zn content. These results collectively highlight the favorable surface characteristics and high-quality crystalline structure achieved in our work.

Conclusion

Zinc-doped $NiFe_2O_4$ nanoparticles ($0 \leq x \leq 0.52$) were synthesized effectively using a hydrothermal method at reduced reaction temperatures and durations. X-ray diffraction (XRD) analysis revealed a decrease in the lattice parameter (D value) from 51 to 37 nm with increasing Zn content. Raman spectroscopy confirmed the presence of five active modes (A1 g + Eg + 3T2 g). High-resolution transmission electron microscopy (HR-TEM) illustrated a cubic structure with an average particle size of 37 nm. Notably, there was a significant increase in the energy bandgap value from 1.57 to 1.96 eV, accompanied by a decrease in crystallite size from 51 to 37 nm. The consistently low dielectric loss observed across the entire frequency range of $Zn_{0.52}$ $Ni_{0.48}$ Fe_2O_4 suggests its potential application in microwave devices. Furthermore, the hysteresis magnetization-field curve exhibited a soft ferromagnetic behavior, accompanied by a notable decrease in saturation magnetization from 98.37 to 75.50 emu/g. These findings collectively underscore the favorable surface characteristics and high-quality crystalline structure achieved in our study. We successfully achieved an enlargement of the band gap to 1.96 eV through our methodology, which involved preparing samples at a low temperature of 180 °C. Additionally, our findings revealed an increase in the magnetic constant K with rising Zn content, in contrast to findings reported in other studies.

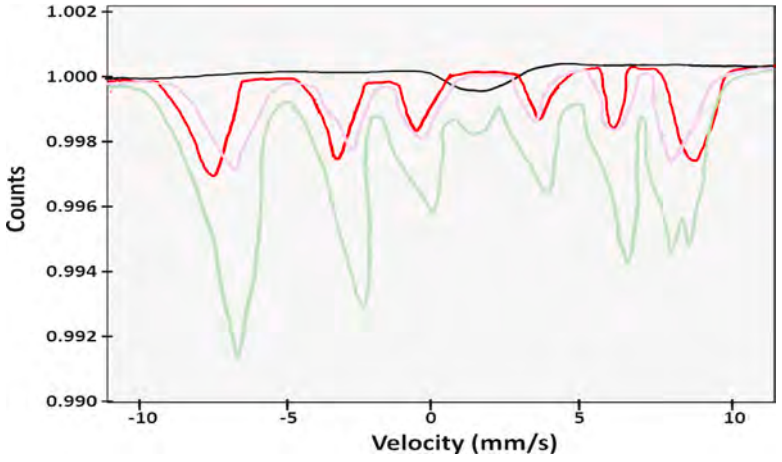

Fig. 9. Mössbauer spectrum of $Zn_{0.52}Ni_{0.48}Fe_2O_4$.

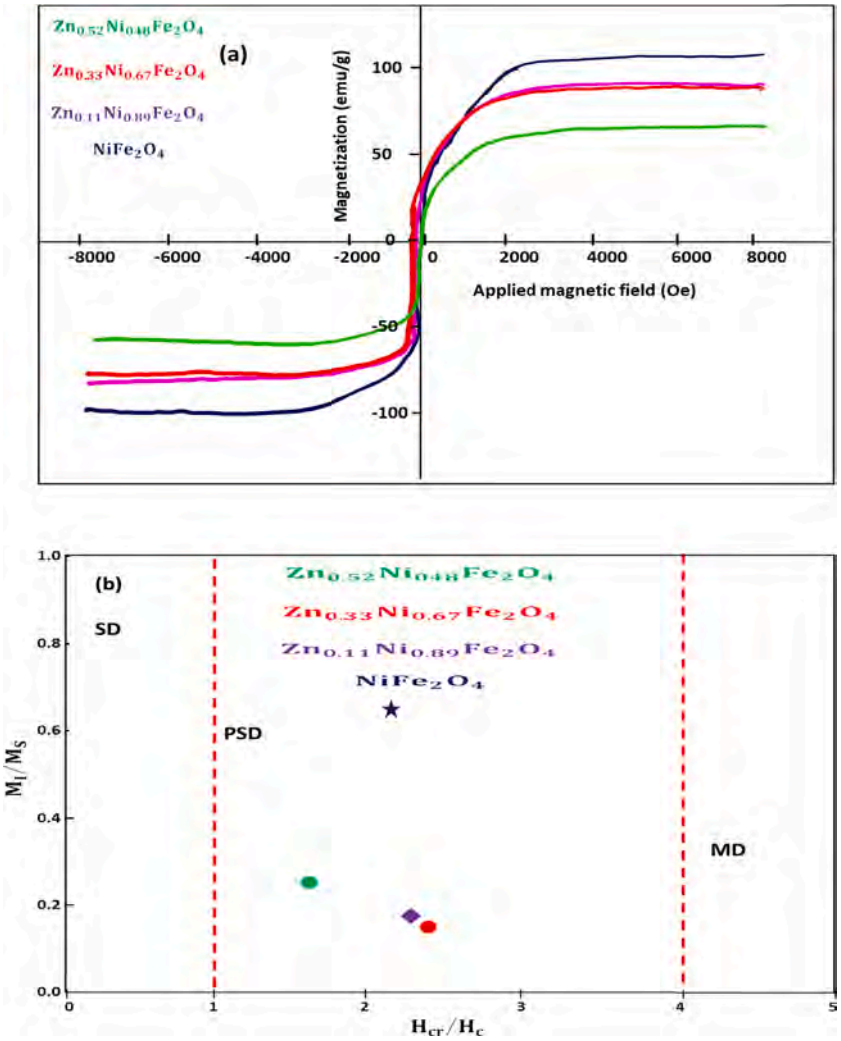

Fig. 10. Room temperature variations of magnetization of $Zn_xNi_{1-x}Fe_2O_4$ nanoparticles with applied magnetic field (a) Hysteresis curve for $x = 0.0$, 0.11, 0.33 and 0.52 and (b) Day plot graph for all samples.

Table 4
Magnetic characteristic of Zn Dopped ferrite nanoparticles ($0 \leq x \leq 0.52$).

Sample	$M_s(emu/g)$	M_r	$H_c(Oe)$	$H_cr(Oe)$	$\frac{M_r}{M_s}$	$\frac{H_cr}{H_c}$	μ_B	$K \times 10^{-3}((emu.Oe)/g)$
$NiFe_2O_4$	98 ± 0.37	11 ± 0.37	45 ± 0.3	115 ± 0.49	0.13	2.5	4.27	4.67
$Zn_{0.11}Ni_{0.89}Fe_2O_4$	92 ± 0.15	13 ± 0.65	50 ± 0.5	123 ± 0.52	0.15	2.46	4.16	5.02
$Zn_{0.33}Ni_{0.67}Fe_2O_4$	87 ± 0.78	13 ± 0.78	56 ± 0.50	130 ± 0.35	0.57	2.32	4.01	5.61
$Zn_{0.52}Ni_{0.48}Fe_2O_4$	75 ± 0.50	13 ± 0.92	82 ± 0.52	144 ± 0.62	0.24	1.7	3.42	6.16

CRediT authorship contribution statement

Eman A. Alghamdi: Conceptualization, Methodology, Validation, Formal analysis, Investigation, Resources, Data curation, Writing – original draft, Writing – review & editing. **Refka Sai:** Conceptualization, Methodology, Validation, Formal analysis, Investigation, Resources, Data curation, Writing – original draft, Writing – review & editing.

Declaration of competing interest

The authors declare that they have no known competing financial interests or personal relationships that could have appeared to influence the work reported in this paper.

Data availability

Data will be made available on request.

Acknowledgment

The authors extend their appreciation to the Deputyship for Research & Innovation, Ministry of Education in Saudi Arabia for funding this research (IFKSUOR3-030-3).

References

[1] Lassoued A, Lassoued MS, Karolak F, Granda SG, Dkhil B, Ammar S, et al. Synthesis, structural, optical, morphological and magnetic characterization of zinc substituted nickel ferrite ($CuxNi1-xFe_2O_4$) through co-precipitation method. J Mater Sci, Mater Electron 2017;28:18480–8.
[2] Shirsath SE, Toksha BG, Jadhav KM. Structural and magnetic properties of In3+ substituted NiFe2O4. J Mater Chem Phys 2009;117:163–8.
[3] Singh S, Singh M, Ralhan NK, Kotnala RK, Verma Kuldeep Chand. Improvement in ferromagnetism of NiFe2O4 nanoparticles with Zn doping. Adv Mat Lett 2012;3(6):504–6.
[4] Shirsath SE, Jadhav SS, Toksha BG, Patange SM, Jadhav KM. Influence of Ce4 + ions on the structural and magnetic properties of NiFe2O4. J Appl Phys 2011;110:013914.
[5] Shirsath SE, Jadhav SS, Toksha BG, Pantage SM, Jadhav KM. Remarkable influence of Ce4+ ions on the electronic conduction of Ni1-2xCexFe2O4. J Scr Mater 2011;64:773–6.
[6] Jadhav SS, Shirsath SE, Toksha BG, Patange SM, Shengule DR, Jadhav KM. Structural and electric properties of zinc substituted NiFe2O4 nanoparticles prepared by co-precipitation method. J Phys B Condens Matter 2010;405:2610–4.
[7] Jagadeesha Angadi V, Kubrin SP, Sarychev DA, Matteppanavar S, Rudraswamy B, Liu H-L, et al. Low temperature Mössbauer spectroscopic studies on Sm 3+ doped Zn-Mn ferrites. J Magn Magn Mater 2017;441:348–55.
[8] Durrani SK, Naz S, Mehmood M, Nadeem M, Siddique M. Structural, impedance and Mössbauer studies of magnesium ferrite synthesized via sol–gel auto-combustion process. J Saudi Chem Soc 2017;21:899–910.
[9] Saxena P, Varshney D. Effect of d -block element substitution on structural and dielectric properties on iron cobaltite. J Alloys Compd 2017;705:320–6.
[10] Choodamani C, Nagabhushana GP, Ashoka S, Prasad BD, Rudraswamy B, Chandrappa GT. Structural and magnetic studies of Mg(1-x)Znx Fe2O4 nanoparticles prepared by a solution combustion method. J Alloys Compd 2013;578:103–9.
[11] Srinivas C, Tirupanyam BV, Meena SS, Yusuf SM, Babu CS, Ramakrishna KS, et al. Structural and magnetic characterization of co-precipitated NixZn1-xFe2o4 ferrite nanoparticles. J Magn Magn Mater 2016;407:135–41.
[12] Bid S, Pradhan SK. Characterization of crystalline structure of ball-milled nano-Ni–Znferrite by rietveld method. Mat Chem Phys 2014;84:291–301.
[13] Abdullah DarJyoti ShahW M, SiddiquiR A, Kotnala K. Study of structure and magnetic properties of Ni–Zn ferrite nano-particles synthesized via co-precipitation and reverse micro-emulsion technique. Appl NanoSci 2014;4(6):675–82.
[14] Paramesh D, Kumar KV, Reddy PV. Effect of aluminium substitution on the electrical properties of Ni-Zn nanoferrites. J Magn Magn Mater 2017;444:371–7.
[15] Ali MA, Uddin MM, Khan MNI, Chowdhury FUZ, Haque SM. Structural, morphological and electrical properties of Sn-substituted Ni-Zn ferrites synthesized bydouble sintering technique. J Magn Magn Mater 2017;424:148–54.
[16] Sudheesh VD, Thomas N, Roona N, Baghya PK, Sebastian V. Synthesis, characterization and influence of fuel to oxidizer ratio on the properties of spinel ferrite MFe2O4, M=Co and Ni prepared by solution combustion method. Ceram Int 2017;43(17):15002–9.
[17] Ghodake JS, Kambale RC, Shinde TJ, Maskar PK, Suryavanshi SS. Magnetic and microwave absorbing properties of Co2+ substituted nickel-zinc ferrites with the emphasis on initial permeability studies. J Magn Magn Mater 2016;401:938–42.
[18] Wang Y, Wu X, Zhang W, Chen W. Synthesis and electromagnetic properties of ladoped Ni-Zn ferrites. J Magn Magn Mater 2016;398:90–5.
[19] Thota S, Kashyap SC, Sharma SK, Reddy VR, Raman Micro. Mossbauer and magnetic studies of manganese substituted zinc ferrite nanoparticles: Role of Mn. J Phys Chem Solids 2016;91:136–44.
[20] Raghasudha M, Ravinder D, Veerasomaiah P, Jadhav KM, Hashim M, Bhatt P, et al. Electrical resistivity and Mössbauer studies of Cr substituted Co nano ferrites. J Alloys Compd 2017;694:366–74.
[21] Ahmad Z, Atiq S, Abbas SK, Ramay SM, Riaz S, Naseem S. Structural and complex impedance spectroscopic studies of Mg-substituted CoFe2O4. Ceram Int 2016;42:18271–82.
[22] Raju K, Venkataiah G, Yoon DH. Effect of Zn substitution on the structural and magnetic properties of Ni-Co ferrites. Ceram Int 2014;40:9337–44.
[23] Atiq S, Majeed M, Ahmad A, Abbas SK, Saleem M, Riaz S, et al. Synthesis and investigation of structural, morphological, magnetic, dielectric and impedance spectroscopic characteristics of Ni-Zn ferrite nanoparticles. Ceram Int 2017;43:2486–94.
[24] Lazarevi Z, Jovaleki A, Daneu Milutinovi N, Rom M, Jovanovi, Rom N. Spectroscopy investigation of nanostructured nickel-zinc ferrite obtained by mechanochemical synthesis. Optoelectron Adv Mater Rapid Commun 2015;9:102–6.
[25] Nordblad Aakash P, Mohan Rajendra, Mukherjee S. Structural, magnetic and hyperfine characterizations of nanocrystalline Zn-Cd doped nickel ferrites. J Magn Magn Mater 2017;441:710–7.
[26] Jagadeesha Angadi V, Kubrin SP, Sarychev DA, Matteppanavar S, Rudraswamy B, Liu H-L, et al. Low temperature Mössbauer spectroscopic studies on Sm 3+ doped Zn-Mn ferrites. J Magn Magn Mater 2017;441:348–55.
[27] Saxena P, Varshney D. Effect of d -block element substitution on structural and dielectric properties on iron cobaltite. J Alloys Compd 2017;705:320–6.
[28] Choodamani C, Nagabhushana GP, Ashoka S, Prasad BD, Rudraswamy B, Chandrappa GT. Structural and magnetic studies of Mg(1-x)Znx Fe2O4 nanoparticles prepared by a solution combustion method. J Alloys Compd 2013;578:103–9.
[29] Srinivas C, Tirupanyam BV, Meena SS, Yusuf SM, Babu CS, Ramakrishna KS, et al. Structural and magnetic characterization of co-precipitated NixZn1-xFe2o4 ferrite nanoparticles. J Magn Magn Mater 2016;407:135–41.
[30] Bid S, Pradhan SK. Characterization of crystalline structure of ball-milled nano-Ni–Znferrite by rietveld method. Mat Chem Phys 2014;84:291–301.
[31] Paramesh D, Kumar KV, Reddy PV. Effect of aluminium substitution on the electrical properties of Ni-Zn nanoferrites. J Magn Magn Mater 2017;444:371–7.
[32] Ali MA, Uddin MM, Khan MNI, Chowdhury FUZ, Haque SM. Structural, morphological and electrical properties of Sn-substituted Ni-Zn ferrites synthesized by double sintering technique. J Magn Magn Mater 2017;424:148–54.
[33] Patil KC, Hegde MS, Rattan T, Aruna ST. Chemistry of nanocrystalline oxide materials: combustion synthesis, properties and applications. Singapore: World Scientific; 2008.
[34] Brand RA. Improving the validity of hyperfine field distributions from magnetic alloys: Part I: Unpolarized source. Nucl Instrum Methods B 1987;28:398.
[35] Jadhav J, Biswas S. Structural and magnetic properties of Znl-xNixO nanoparticles synthesized by a wet chemical method. Appl Mech Mater 2013;446–447:137–41.
[36] Abdullah Dar M, Majid K, Batoo KM, Kotnala RK. Dielectric and impedance study of polycrystalline li0.35-0.5XCd0.3NiXFe2.35-0.5XO4 ferrites synthesized via a citrategel auto combustion method. Elsevier B.V.; 2015.
[37] Rao BP, Caltun OF. Microstructure and magnetic behaviour of Ni-Zn-Co ferrites. J Optoelectron Adv Mater 2006;995–7.
[38] Randhawa BS, Dosanjh HS, Kaur M. Preparation of ferrites from the combustion of metal nitrate-oxalyl dihydrazide solutions. Indian J Eng Mater Sci 2005;12:151–4.
[39] Costa ACFM, Tortella E, Morelli MR, Kiminami RHGA. Synthesis, microstructure and magnetic properties of Ni-Zn ferrites. J Magn Magn Mater 2003;256:174–82.

[40] Magnetism N, View P, View I. Structural and dielectric properties of copper-. J Supercond Nov Magn 2016;1–6.
[41] Da Dalt S, Takimi AS, Volkmer TM, Sousa VC, Bergmann CP. Magnetic and Mössbauer behavior of the nanostructured MgFe 2 o 4 spinel obtained at low temperature. Powder Technol 2011;210:103–8.
[42] Singh JP, Srivastava RC, Agrawal HM, Kumar R. Micro-Raman investigation of nanosized zinc ferrite: Effect of crystallite size and fluence of irradiation. J Raman Spectrosc 2011;42:1510–7.
[43] De M, Rout A, Tewari HS. Synthesis and Structural Characterization of A-site Doped, vol. 40042, 2017, p. 4–8.
[44] Nordblad Aakash P, Mohan Rajendra, Mukherjee S. Structural, magnetic and hyperfine characterizations of nanocrystalline Zn-Cd doped nickel ferrites. J Magn Magn Mater 2017;441:710–7.
[45] Salah LM. Spectroscopic studies of the effect of addition of Y 3+ on structural characteristics of Ni-Zn ferrites. Phys Status Solidi 2006;203:271–81.
[46] Ahlawat A, Sathe VG, Reddy VR, Gupta Ajay, Mossbauer. Raman and X-ray diffraction studies of superparamagnetic NiFe2O4 nanoparticles prepared by sol–gel auto-combustion method. J Magn Magn Mater 2011;323:2049–54.
[47] Chandramohan P, Srinivasan MP, Velmurugan S, Narasimhan SV. Cation distribution and particle size effect on Raman spectrum of CoFe2O4. J Solid State Chem 2011;184:89–96.
[48] Wang Z, Lazor P, Saxena SK, St H, Neill CO. High pressure Raman spectroscopy of. Mater Res Bull 2002;37:1589–602.
[49] Inbanathan SSR, Vaithyanathan V, Arout Chelvane J, Markandeyulu G, Kamala Bharathi K. Moossbauer studies and enhanced electrical properties of R (R=Sm, Gd and Dy) doped Ni ferrite. J Magn Magn Mater 2014;353:41–6.
[50] Jiang NN, Yang Y, Zhang YX, Zhou JP, Liu P, Deng CY. Influence of zinc concentration on structure, complex permittivity and permeability of Ni-Zn ferrites at high frequency. J Magn Magn Mater 2016;401:370–7.
[51] Shinde SS, Meena SS, Yusuf SM, Rajpure KY. Mossbauer, Raman and magnetoresistance study of aluminum-based iron oxide thin films. J Phys Chem C 2011;115:3731–6.
[52] Praveena K, Srinath S. The effect of Sb on the electrical and magnetic properties of Ni- Zn ferrites prepared by sol–gel autocombustion method. J Electroceramics 2013;31:168–75.
[53] Wu KH, Ting TH, Yang CC, Wang GP. Effect of complexant/fuel on the chemical and electromagnetic properties of SiO2-doped Ni–Zn ferrite. Mater Sci Eng B 2005;123:227–33.
[54] Priyadharsini P, Pradeep A, Rao PS, Chandrasekaran G. Structural, spectroscopic and magnetic study of nanocrystalline Ni-Zn ferrites. Mater Chem Phys 2009;116:207–13.
[55] Thakura Sangeeta, Katyal SC, Singh M. Structural and magnetic properties of nano nickel–zinc ferrite synthesized by reverse micelle technique. J Magn Magn Mater 2009;321:1–7.
[56] Dippong Thomas, Cadar Oana, Andrea Levei Erika, Bibicu Ion, Diamandescu Lucian, Leostean Cristian, et al. Structure and magnetic properties of CoFe2O4/SiO2 nanocomposites obtained by sol–gel and post annealing pathways. Ceram Int 2017;43(2):2113–22.
[57] Dippong T, Levei EA, Deac IG, Petean I, Cadar O. Dependence of structural, morphological and magnetic properties of manganese ferrite on Ni-Mn substitution. Int J Mol Sci 2022;23:3097.
[58] Ştefănescu M, Dippong T, Stoia M, Ştefănescu O. Study on the obtaining of cobalt oxides by thermal decomposition of some complex combinations, undispersed and dispersed in SiO2 matrix. J Therm Anal Calorim 2008;94(2):389–93.
[59] Dippong Thomas, Andrea Levei Erika, Leostean Cristian, Cadar Oana. Impact of annealing temperature and ferrite content embedded in SiO2 matrix on the structure, morphology and magnetic characteristics of (Co0.4Mn0.6Fe2O4) and (SiO2)100- nanocomposites. J Alloys Compounds 2021;868:159203.
[60] Dippong Thomas, Levei Erika-Andrea, Toloman Dana, Barbu-Tudoran Lucian, Cadar Oana. Investigation on the formation, structural and photocatalytic properties of mixed Mn-Zn ferrites nanoparticles embedded in SiO2 matrix. J Anal Appl Pyrolys 2021;158:105281.
[61] Dippong Thomas, Andrea Levei Erika, Goga Firuta, Cadar Oana. Influence of Mn2+ substitution with Co2+ on structural, morphological and coloristic properties of MnFe2O4/SiO2 nanocomposites. Mater Character 2021;172:110835.
[62] Dippong Thomas, Toloman Dana, Dan Monica, Andrea Levei Erika, Cadar Oana. Structural, morphological and photocatalytic properties of Ni-Mn ferrites: Influence of the Ni:Mn ratio. J Alloys Compd 2022;913:165129.
[63] Dippong T, Levei EA, Deac IG, Petean I, Borodi G, Cadar O. Sol-gel synthesis, structure, morphology and magnetic properties of Ni0.6Mn0.4Fe2O4 nanoparticles embedded in SiO2 matrix. Nanomaterials 2021;11:3455.
[64] Anupama MK, Srinatha N, Matteppanavar Shidaling, Angadi Basavaraj, Sahoo Balaram, Rudraswamy B. Effect of Zn substitution on the structural and magnetic properties of nanocrystalline $NiFe_2O_4$ ferrites. Ceram Int 2017. 12.087.